International Journal of Adhesion & Adhesives 120 (2023) 103292

Contents lists available at ScienceDirect

International Journal of Adhesion and Adhesives

journal homepage: www.elsevier.com/locate/ijadhadh

Optimisation of interlocking microstructured adhesive joints via finite element modelling, design of experiments and 3D printing

Alex Hamilton [a], Yang Xu [b,**], Mehmet E. Kartal [c], S. Kumar [a], Nikolaj Gadegaard [a], Daniel M. Mulvihill [a,*]

[a] James Watt School of Engineering, University of Glasgow, Glasgow, G12 8QQ, UK
[b] School of Mechanical Engineering, Hefei University of Technology, 230009, China
[c] School of Engineering, University of Aberdeen, Aberdeen, AB24 3UE, UK

ARTICLE INFO

Keywords:
Micro structuring
Interlocking
Single lap joint
Micro-fabrication
Injection moulding
3D printing

ABSTRACT

The potential to optimise the performance of microstructured joints based on mechanically interlocking adherends is investigated via experimental testing and finite element (FE) analysis. The microstructured joints were realised via imprint lithography and injection moulding. FE modelling indicated that, a frictional interface (i.e. no adhesive) was sufficient to generate joint load capacities within about 7% of the experimental values. This result indicates that mechanical interlocking (via feature bending) accounts for most of the tangential load carrying capacity of the joints – opening up the possibility of adhesive-less joints. The FE model was then used for a design of experiments analysis to identify key relationships between interlocking geometric parameters and mechanical performance, with a three-way ANOVA analysis employed to determine relative importance. Feature aspect ratio was found to be the key parameter defining performance. Energy absorption increased with feature aspect ratio while load capacity peaked at an aspect ratio of 1 making square features the best compromise for load capacity and toughness. Finally, the viability of a more cost-effective, SLA-based 3D printing approach is demonstrated for fabricating the interlocking joints, whereby the potential to tailor for optimised hybrid performance was studied by varying feature geometry horizontally along the joint.

1. Introduction

Adhesive bonding is a highly promising approach to joining components due to their ease of assembly and removal of the need to machine holes for mechanically fastened joints. Although adhesive joining is a lightweight and simple solution, mechanical properties are not as reliable as with traditional mechanical fixation. One of the main drawbacks of bonded joints is their susceptibility to unpredictable failure via crack propagation in response to sudden impact loads for example – this is the reason for the hesitance surrounding their use in safety-critical aerospace applications. Hence, approaches to concurrently increase both strength and toughness are highly desirable. Conventionally, adhesive joints are comprised of overlapping planar adherends and are limited by the properties of the adhesive layer and by the nature of the classical peel and shear stress distributions that produce very high peak stresses near the edges. Making the overlap region longer does not markedly improve performance as failure is usually governed by Mode I crack opening due to the high peel stresses near the edges. Apart from making the adhesive stronger, there are a number of other approaches that have been used successfully to improve mechanical properties. One of these is to impart particular roughness or structuring on the adherends to ensure a better interlock between adherend and adhesive. With regard to improving the surface properties of metallic adherends, considerable attention has centred on the use of the laser ablation technique, where material removal imparts a microstructured topography enabling adhesive interlock and increasing strength and toughness [1–3]. With a concerted effort to reduce weight in bonded structures such as in automotive and aerospace applications, efforts have also been made to study composite based joining methods. Innovative fabrication approaches facilitating the joining of fibre reinforced plastics have been studied, enabling the production of interfaces possessing high strength-to-weight ratios [4,5]. However, on account of possessing lower surface energies, polymer-based adhesive joints typically possess lower bond strength compared to metallic joints, but there are other

* Corresponding author.
** Corresponding author.
E-mail addresses: yang.xu@hfut.edu.cn (Y. Xu), Daniel.Mulvhilll@glasgow.ac.uk (D.M. Mulvihill).

https://doi.org/10.1016/j.ijadhadh.2022.103292
Received 23 May 2022; Received in revised form 27 September 2022; Accepted 29 October 2022
Available online 2 November 2022

approaches that can be deployed to assist and mitigate this issue.

Within the context of polymer based single lap joints, novel 3D printing approaches have been developed recently to spatially vary the compliance of either the adhesive [6] or the adherends [7] along the bond line. Tailoring to produce a reducing stiffness in higher stressed regions (i.e. near the edges) was found to reduce peak stresses and confer enhanced strength and toughness properties. Another important approach (the one which we focus on here) is surface structuring to produce joints based on mechanically interlocking adherends (as opposed to just interlock between adhesive and adherend). This has been explored relatively recently by a number of researchers as a promising route to increasing strength and toughness. The work of Maloney and Fleck [8], for example, has illustrated the benefits of a an interlocking square wave architecture on the performance of both millimetre structured butt joints (in normal separation) and double cantilever beam joints (under Mode I loading) [8,9]. Enhanced mechanical properties were observed in this case because the sides of the square-wave features introduce an important degree of shear mode loading which is inherently stronger than the normal loading found in the separation of butt joints with nominally planar surfaces. Research addressing the double cantilever beam was carried out by Cordisco et al. [10] who tested sinusoidal patterns in adherends composed of aluminium alloy. Load-displacement graphs indicated that the fracture pathway is delayed with the features introducing an intermittent crack propagation with a 'stick-slip' behaviour yielding greater energy absorption. Corbett et al. [11] have shown that a single lap joint (SJL) setup composed of a single interlocking feature in shear demonstrated considerable improvements (up to 86.5%) in work-to-failure. Additional work by the same authors looking at optimising feature geometry lead to work-to-failure increases of up to 542% [12]. The work-to-failure here was mainly boosted by a much more prolonged fracture process as fracture has to progress around the features (rather than the rapid straight-line progression of cracks in planar SLJs). Ramaswamy et al. [13] deployed interlocking features (tapered square wave) in the single lap bonding of metal and carbon fibre reinforced composite material. They noted a 10% increase in lap shear strength and a 75–120% increase in work-to-failure in tests across a range of loading rates. In Hahgpanah et al. [14], V-shaped teeth-like profiles in steel (at each edge of the bond line only) were shown to dramatically modify the failure mechanism of the SLJ giving a strength increase of 12% and an energy absorption increase of roughly 100% relative to planar samples. They also found significant potential of the features to arrest cracks and redistribute stresses. Further examples of interlocking adhesive joints can be seen in the in-mould surface preparation of CFRP laminates tested in Mode I and Mode II crack opening tests, leading to marked improvement in fracture toughness for both loading regimes [15,16].

In our recent work (Hamilton et al. [17]), the scope of the interlocking adherend work was expanded by developing an alternative adhesive single lap joint comprising micron scale interlocking square wave microfeatures within polycarbonate adherends. This was achieved via a photolithography based microfabrication approach in conjunction with injection moulding [18] (this methodology was also deployed recently in studies of the friction [19] and contact stiffness [20] of non-bonded interfaces). For the bonded interlocking interfaces, mechanical strength and work-to-failure improved by up to 95% and 162% relative to benchmark roughened planar specimens, respectively. In-situ testing revealed that progressive bending resistance at each interlocking square-wave feature pair appeared to confer the enhanced mechanical properties. Feature bending is able to develop greater load resistance as well as permit more displacement resulting in a stronger and tougher joint. Toughness is also likely to be boosted by the more tortuous crack path that the square-wave interface confers. These results highlighted the potential of mechanically interlocking joints for more widespread use in boosting mechanical performance. Since the interlocking geometries are on the micron scale, interfaces could be redesigned without effecting the macroscale geometry of components. However, to better understand and maximise the performance of these joints, a more focused optimisation study is required. The present study builds on the previous experimental work by first developing a representative finite element (FE) model of the interlocking joint. This is then used to compare directly with a set of experiments and used further in an optimisation study to ascertain the optimal micron scale geometries for joint performance. Finally, approaches to tailoring feature geometry and dimensions for optimum properties using more rapid 3D printing approaches are explored and tested.

2. Finite element model

The first step in the optimisation was to develop a representative FE model of the square-wave polycarbonate structured single lap joints of the type developed in Hamilton et al. [17]. ABAQUS Implicit (2017) was used to develop a model of the joint. A static, 2D plane-strain model was constructed as it was assumed that through-thickness effects, due to having a uniform profile, were considerably less important and that the plane of interest is sufficiently far from the free surface condition in the thickness direction. Fig. 1 shows a schematic of the model. Linear, reduced integration, plane strain elements (CPE4R) were used for the adherends with a surface-to-surface interaction between the micro-features defining the contact relationship. The mesh was seeded to be coarser at regions distal to the bond-line for computational time-efficiency with the mesh becoming suitably refined at the articulating micro features. Part geometries were kept the same as in Hamilton et al. [17] with the adherends designed with dimensions of 40 mm x 10 mm and a bond-line length of 7.5 mm. The boundary conditions implemented replicate the experiment with one end of the lap joint fixed and displacement applied at the opposite end. A boundary condition $U_y = 0$ was applied to the top surfaces of the adherends to prevent vertical displacement to replicate the particular way in which the joints in Ref. [17] were constrained (i.e. bonded to a relatively rigid backing support that could only move laterally). This boundary condition from the experiment is somewhat unusual. It was necessitated by the need to prevent the thin adherends in Ref. [17] from fracturing. In practice, it also substantially mitigates the eccentric bending of the single lap joint due to the bending moment emanating from the asymmetric setup.

Surface to surface contact was used to define the frictional contact relationship, with the upper adherend surface assigned as the master and the lower adherend assigned as the slave surface. Within the analyses, small sliding formulation was selected, a penalty friction formulation and hard normal contact property were selected to govern tangential and normal contact behaviour respectively.

The polycarbonate was modelled as an elastic-plastic material with Young's modulus, $E = 2.6$ GPa and Poisson ratio, $\nu = 0.32$. The plastic behaviour of the polycarbonate was modelled using Johnson-Cook data obtained in Ref. [21]. Since no failure of the polycarbonate was observed in the experiments (Hamilton et al. [17]), no failure initiation or damage criteria were applied to the polycarbonate. Table 1 provides a summary of the Johnson-Cook hardening data used according to the parameters in the Johnson-Cook isotropic hardening equation:

$$\sigma^o = \left(A + B\varepsilon^{pl}\right)^n, \tag{1}$$

where parameters A and B are the initial yield stress of the material and the strain hardening stress coefficient of the material respectively; the term ε^{pl} represents the equivalent plastic strain and the parameter n is the strain hardening coefficient. The Johnson-Cook model can account for temperature-effects, however since the simulations aimed at modelling loading at room temperature (well below the transition temperature for polycarbonate) this term was omitted from the equation. Likewise, strain rate dependence was not factored into the model.

Since we would like to determine how much of the load carrying resistance of this specific joint configuration is due to mechanical interlocking (as opposed to adhesive strength), it was decided to initiate

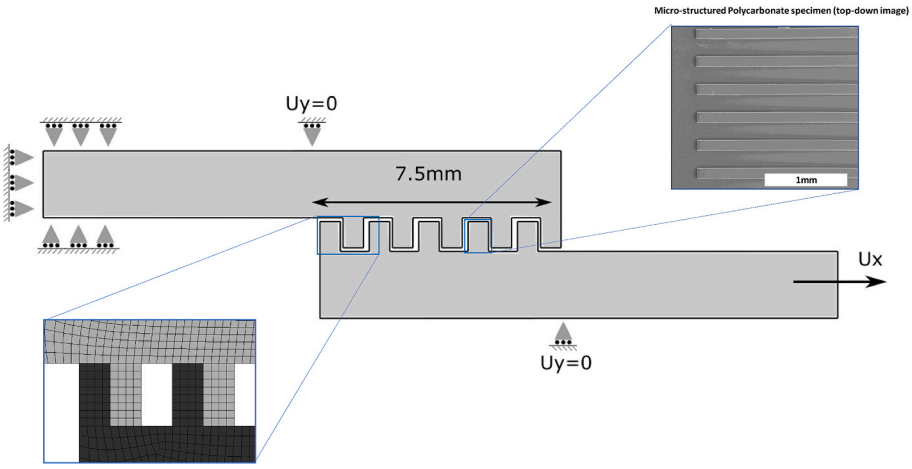

Fig. 1. Schematic of the FE model indicating the geometry and boundary conditions with no adhesive present in the model (i.e. frictional contact only). The left-hand side was fixed whilst displacement was applied at the right-hand end of the joint. Boundary conditions were imposed to constrain vertical displacement on the top and bottom surfaces (as shown) to simulate the experimental testing conditions in Hamilton et al. [17]. A close-up image of the refined mesh at the micro-features is provided in the bottom left with frictional contact defined at the points of contact between the sidewalls of each discrete feature. The magnified image (top-right) shows the fabricated square-wave features in the polycarbonate adherends.

Table 1
Johnson-Cook empirically-derived parameters (from Ref. [21]).

A (MPa)	75.8
B (MPa)	68.9
n	1.004

the modelling using frictional contact of the interlocking teeth instead of the common cohesive element-based approach to modelling of adhesive interfaces. Comparison with experimental results was used to verify the scope of the proposed approach. Suitable values for the coefficient of friction and maximum shear stress for polycarbonate were taken from the literature [22] (values of 0.31 and 30 MPa were selected, respectively). As can be seen in Fig. 2, there are some notable variables to consider when designing the prospective interlocking joint profile. These variables include the feature width (λ_f), channel width (λc) and depth (D) and aspect ratio (AR). The geometric variables were studied in various setups to gain greater insight into interlocking joint performance.

3. Results and discussion

3.1. Comparison of model and experiment

To enable direct comparison with the model, experiments were conducted to study the effect of feature width on the joint performance, with feature widths of 50 μm and 100 μm used for testing. The micro-structured interfaces were produced using the micro-fabrication and injection moulding protocol utilised in the previous study and polycarbonate was retained as the adherend material [18]. During the micro-fabrication process, anisotropic reactive ion etching was utilised to define the feature height in the silicon master. Through careful selection of the etch time, a height of 50 μm was produced enabling aspect ratios of 1 and 0.5 to be realised for each of the designed feature widths. Channel width was chosen as 1.5 times the feature width for all test samples. An SEM image of the final structured polycarbonate surface is included in Fig. 1. Samples were bonded using the two-part epoxy (Araldite Rapid) and cured for 4 h according to the manufacturer's guidelines. For each feature width, a total of five repeat tests was performed. Testing was conducted using a Deben micro-tester with a modified test rig (developed in Hamilton et al. [17]) and designed to prevent wholescale bending and fracture of the thin polycarbonate. An annotated photograph is given in Fig. 3, illustrating the test setup. Testing was performed under an extension rate of 0.5 mm/min with localised strain for the joints calculated between the outer edges of the bond-line using digital image correlation (DIC) software (Imetrum, UK). The mean failure loads, strain-to-failure and work-to-failure for each group are given in the bar graph plots in Fig. 4.

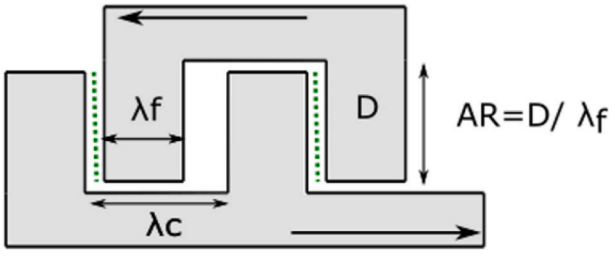

Fig. 2. Schematic highlighting the key geometric properties for the interlocking joint profile: feature width (λf), channel width (λc), channel depth (D) and aspect ratio (AR).

Overall, there is reasonable agreement between model and experiment. For the 0.5 aspect ratio group, the simulations over predict relative to the experiments by 6.9%, 11.9% and 43.5% for load capacity, strain-to-failure and work-to-failure, respectively. For the 1.0 aspect ratio group, the simulations typically under-predict by 12.7%, 29.8% and 45%, respectively. The frictional model (i.e. no adhesive present) is a largely good predictor of load capacity (results are within +6.9 to −12.7% of the mean experimental test results). This is an important finding as it validates the concept that the adherends primarily resist the majority of the elevated loading via mechanical interlocking. Hence, in the case of load capacity, we can conclude that the adhesive plays rather a secondary role. In theory, this opens up the possibility of adhesive-less joints as long as sufficient lateral constraint is maintained to hold the joint together (such as by clamping the joint). Greater discrepancies between model and experiment are apparent for strain-to-failure and work-to-failure. This variability was attributed to the failure modes occurring in the experiments possessing an element of variability on account of the geometric variation during the assembly of the joint. For example, for AR = 0.5 group (Fig. 4b and c), the simulated strain-to-failure and work-to-failure are over-predicted by 11.9% and 43.5%. This finding can largely be attributed to the experimental AR = 0.5 case fracturing at slightly lower displacements via an adhesive dominant failure because effective interlocking was less facile to achieve in practice.

On the other hand, for the AR = 1.0 case (Fig. 4e and f), the model under predicted strain-to-failure and work-to-failure by 29.8% and 45%, respectively. Here, the micro-structured joints are interlocked to a greater degree. Under this circumstance, the presence of the adhesive (in the experiments) can act alongside the greater interlocking to offer additional resistance to failure at the later stages of joint elongation, facilitating a more prolonged failure.

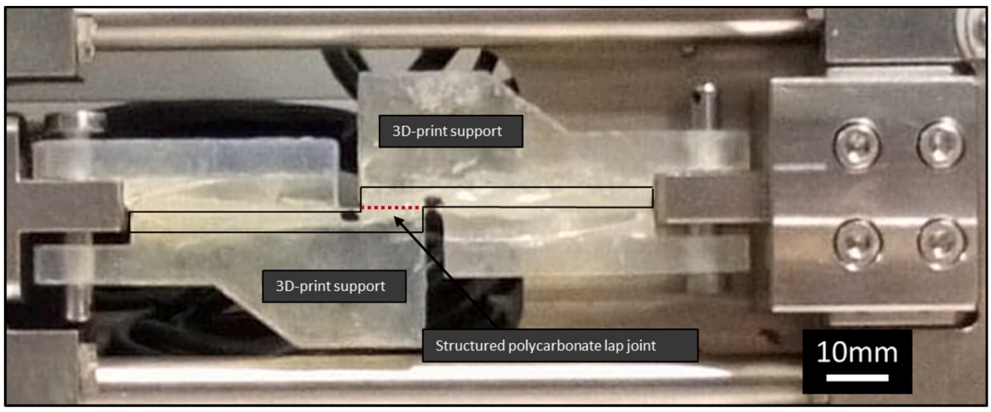

Fig. 3. Photograph of the mechanical testing setup for joint testing: The 3D printed supports provide mechanical rigidity to mitigate bending of the joint (and fracture of the thin polycarbonate samples). The black outline illustrates the position of the structured polycarbonate test specimen with the dotted line illustrating the location of the structured interface.

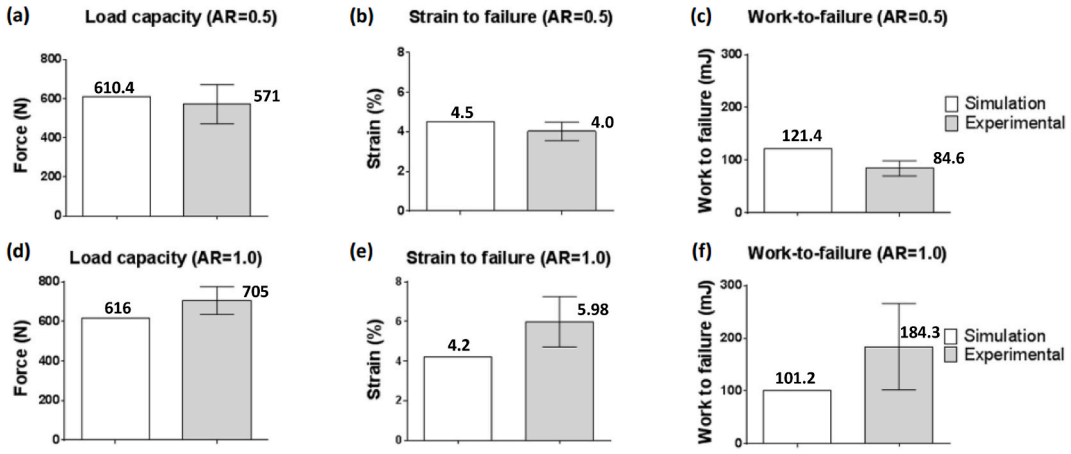

Fig. 4. Comparison of finite element model (white) with mean experimental results (grey) according to load capacity (left), strain-to-failure (middle) and work-to-failure (right) for: (a–c) Aspect ratio (AR) = 0.5 and (d–f) Aspect ratio (AR) = 1.0. Experimental results are based on $n = 5$ test results.

Based on the results we can conclude that the model is a good predictor of joint load capacity, whereas there is more disagreement associated with the strain-to-failure and work-to-failure values relative to the experiments. However, it is reasonable to conclude that the model will still be an effective predictor of overall trends when geometries of the micro-topography are varied. More accurately modelling strain-to-failure and work-to-failure for the interlocking square-wave setup with the incorporation of interfacial cohesive elements would not be straightforward and remains a prospective challenge for future work. It should be noted that higher aspect ratios (>1.0) were not tested due to complications associated with the micro-fabrication process (i.e. difficulty in creating high fidelity features). As highlighted previously, the localised mechanical loading of the micro-features has been imaged in-situ in a previous work [17], where discrete feature bending was shown to provide enhanced mechanical resistance owing to the interlocking nature of the bond-line and the particular boundary conditions used. Load-displacement plots with corresponding evolution of feature deformation and bending are also given in Ref. [17].

3.2. Optimisation of joint design using design of experiments (DoE)

The main drawback of a purely experimental methodology is the relatively low throughput, leading to difficulties in testing a wide range of prospective micro-structured joint designs. The key advantage of finite element modelling is the ability to perform simulations for a high number of tests, with economical use of time and resources. Therefore, the frictional model outlined in the previous section was used in a design of experiments (DoE) protocol to ascertain the relationships between the key geometrical parameters as well as to determine the geometries yielding the greatest load capacities. In this study, the Taguchi analysis method was employed to expedite the optimisation process. The Taguchi method is primarily used within the manufacturing sector to optimise processes to increase yield as well as minimise variation in final products [23].

Fundamentally, the process of interest is broken down into the main contributing factors with levels assigned to each factor accordingly. Experiments can be subsequently conducted with a range of factor values tested in an orthogonal array format. The response of the dependent variables is assessed for each experiment and the importance of each factor can be identified. Within the context of optimising the structured joint performance, three geometrical variables were assigned as the control factors for the testing: feature width (λ_f), relative channel width (λ_c) and aspect ratio (AR) (see Fig. 2). Three response factors were outlined as load capacity, strain-to-failure and work-to-failure. Three feature widths were selected as 50, 75 and 100 μm; widths were chosen as multiples of 1.25, 1.5 and 2.0 relative to the feature width and aspect ratios of 0.5, 1.0 and 2.0 were tested. A total of 27 models were generated and run to fulfil the testing outlined in Table 2. The simulation plots are given in Fig. 5 with the three separate rows of plots representing a discrete feature width of 50 μm (Fig. 5a–c), 75 μm (Fig. 5d–f) and 100 μm (Fig. 5g–i).

Looking collectively at the data in Fig. 5, it is evident that there are

Table 2
Orthogonal array of testing for the Taguchi analysis method.

Test No.	Feature width (μm)	Channel width (μm)	Aspect ratio (AR)	Test No.	Feature width (μm)	Channel width (μm)	Aspect ratio (AR)
1	50	63	0.5	15	75	113	2
2	50	63	1	16	75	150	0.5
3	50	63	2	17	75	150	1
4	50	75	0.5	18	75	150	2
5	50	75	1	19	100	125	0.5
6	50	75	2	20	100	125	1
7	50	100	0.5	21	100	125	2
8	50	100	1	22	100	150	0.5
9	50	100	2	23	100	150	1
10	75	94	0.5	24	100	150	2
11	75	94	1	25	100	200	0.5
12	75	94	2	26	100	200	1
13	75	113	0.5	27	100	200	2
14	75	113	1				

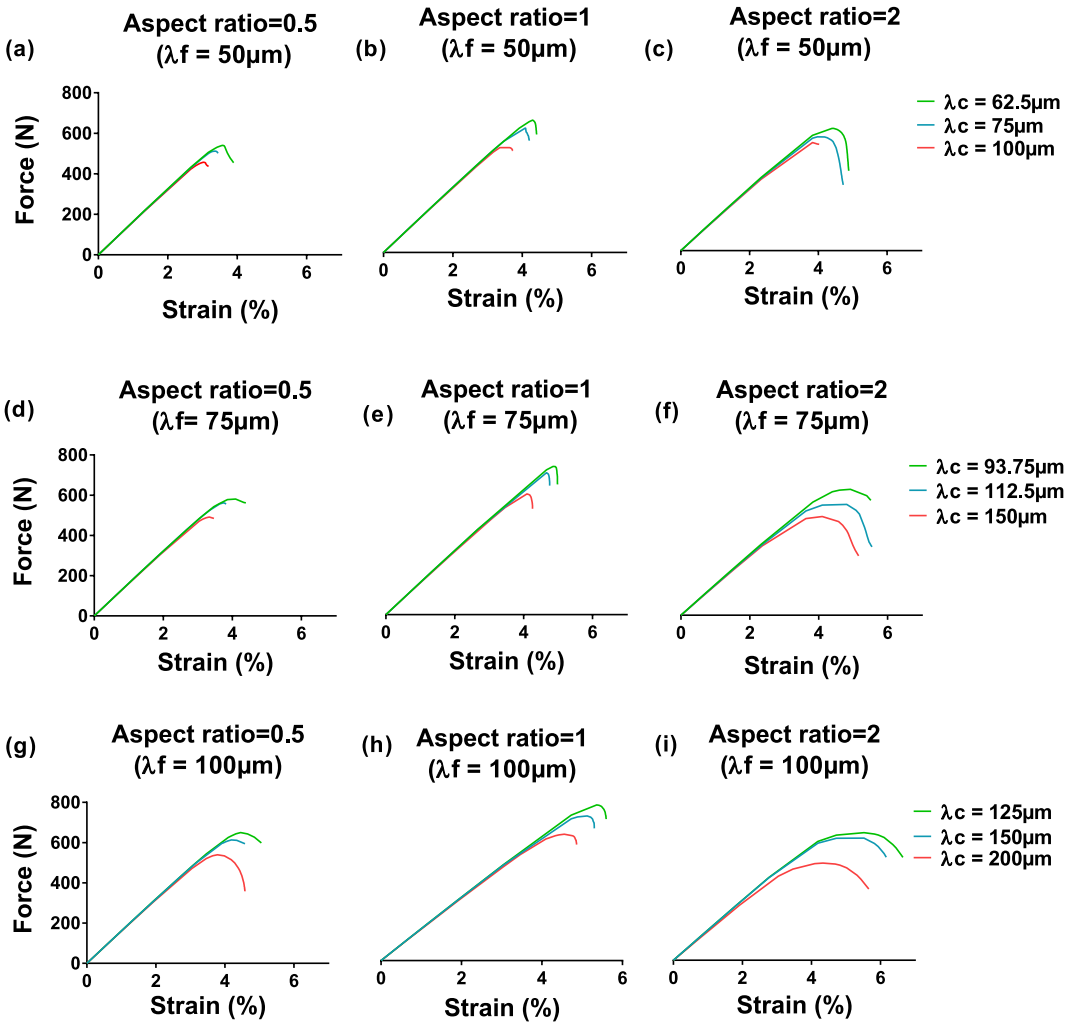

Fig. 5. Force-strain data for all simulations; (a–c) represents results for the 50 μm feature width group; (d–f) represents the 75 μm feature width group and (g–i) represents the 100 μm feature width group. The values in the legends are channel widths.

key relationships that exist between the geometric parameters, although the dependence of each cannot be easily determined from the plots. The Taguchi analysis enables the response variables (load capacity, strain-to-failure and work-to-failure) to be measured for each factor using the signal to noise equation given as:

$$\frac{S}{N} = -10\left(\frac{1}{n}\right)\sum_{i=1}^{n}\frac{1}{y_i^2}, \tag{2}$$

where y is the responses for the given factor level combination and n = number of responses in the factor level combination. In this case, $n = 1$ was used. The statistical analysis was performed using Minitab statistical analysis software. Since the objective of the study is to maximise the values calculated for load capacity, strain-to-failure and work-to-failure, the larger the signal-to-noise ratio variant of Taguchi analysis was utilised. The main effects plots for each independent variable are given in Fig. 6, with plots for load capacity (Fig. 6a–c), strain-to-failure

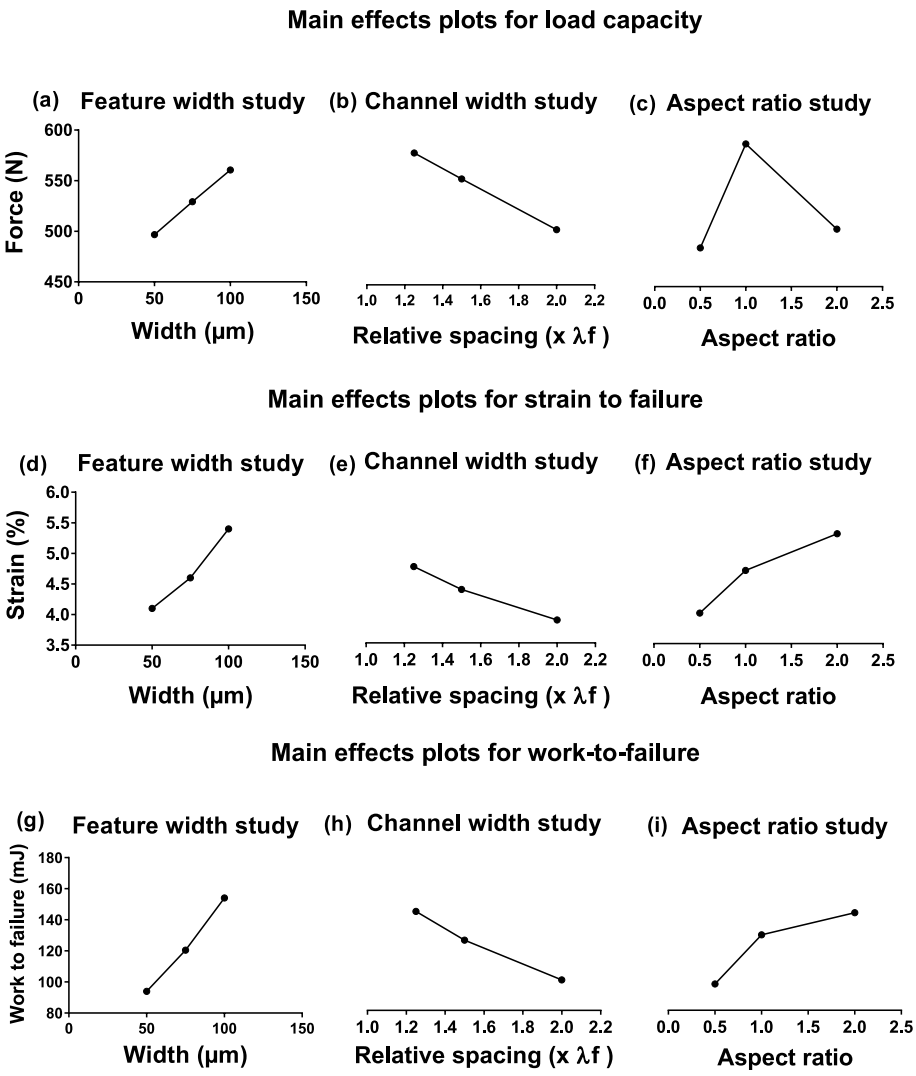

Fig. 6. Main effects plots for the average loads for each factor level: (a–c) corresponds to the maximum load, (d–f) corresponds to the strain-to-failure and (g–i) corresponds to the work-to-failure results.

(Fig. 6d–f) and work-to-failure (Fig. 6g–i) shown. It should be noted that, within the main effects plots, the channel width values were grouped and plotted as multiples of feature width (λ_f), i.e. 1.25, 1.5 and 2 times the feature width value (λf).

The main effects plots provide some definitive trends between geometrical parameters. For example, load capacity increases roughly proportional to feature width. This result is intuitive since increases in feature width will lead to a larger bending stiffness associated with each micro-feature, thus allowing greater loads to be transmitted for a given joint displacement. On the other hand, load capacity decreased roughly proportionally to channel width. Again, this result is expected since an increase in channel width leads to a reduction in feature density. Lower feature density leads to less feature per unit area, leading to a higher proportion of loading being transmitted through each interlocking unit resulting in premature failure. For aspect ratio (AR), load capacity has an intermediate peak at AR = 1.0 (Fig. 6c). At AR = 0.5, the result was lower due to difficulties in achieving effective interlocking, whereby even under vertically constrained boundary conditions, a small element of adherend rotation will have a dramatic effect on how effectively lower depth features can transmit load via compression. This was identified as the primary reason that limited the ability for the lower aspect ratio features to effectively resist higher loads. When aspect ratio is increased to 2.0, load capacity also drops off again and this is likely due to the reduced stiffness of the higher aspect ratio features (i.e. longer thinner features). On the other hand, both strain-to-failure and work-to-failure increase with increasing aspect ratio (Fig. 6f and i). This is because, as the stiffness of the features reduces, they permit more bending deformation. Thus, the optimum result in terms of optimising total load capacity and work-to-failure was found to be the 1.0 aspect ratio case. In summary, the optimal results occurring at the intermediate aspect ratio (AR = 1) can be explained through two conflicting phenomena. Lower aspect ratios will have a greater resistance to bending associated with each feature whilst the higher aspect ratio features enable greater bending prior to joint separation (so greater strain and work done).

3.3. Analysis of variance (ANOVA)

To supplement the Taguchi analysis, a three-way ANOVA analysis was performed to successfully quantify the percentage contribution of the control factors as well as determining if there are any significant interactions between parameters. The ANOVA is a powerful statistical tool with many applications within various sectors although it is typically a tool employed by the manufacturing industry. ANOVA analysis requires the variance to be calculated within each variable group as well as in between each group. An *F*-ratio was calculated at 95% confidence

interval with the relative contribution of each variable determined. The results for the three-way ANOVA are given in Table 3.

Reviewing the *p*-values associated with each independent variable, it is clear that the very low values close to zero indicate that we can reject the null hypothesis and conclude that each geometrical factor is crucial to the final result. The key variable of percentage contribution is obtained for each geometric parameter by dividing each discrete sum of squares (SS) by the total sum of squares for the dataset.

Considering the contribution of each parameter to load capacity individually, the aspect ratio is the major effecting factor with approximately 40.1% contribution. The channel width is the second most effecting factor with 35.4% contribution while feature width results in a smaller relative contribution of 13.7%. These results illustrate that the optimal joint design prioritises an aspect ratio of 1.0 whilst, tighter fitting, wider features are a secondary design consideration.

The ANOVA analysis results for strain-to-failure are notably different. Again, the low *p*-values indicate that the null hypotheses can be rejected. Logically, the aspect ratio was a major effecting geometric factor, with 39.4% contribution. This time, feature width was the most prominent factor with a 44.8% contribution and channel width had a 12.4% contribution to the result. The strain results demonstrate that a compromise between load capacity (AR = 1) and strain-to-failure (AR = 2) has to be considered. ANOVA analysis results for the work-to-failure values re-affirm that feature width is the primary factor with approximately 44.7% contribution. Channel spacing and aspect ratio resulted in contributions of 24.1% and 27.3%, respectively. The improvements in attainable joint load capacity through the optimisation protocol are considerable. Based on the lap joint dimensions and the quoted maximum joint stress for a polycarbonate lap joint using Araldite rapid adhesive, a maximum load of approximately 225 N was calculated. In this study, a maximum load capacity of 773.9 N was obtained equating to a 244% increase in load capacity [24].

It should be emphasised that the substantial improvements in load capacity and toughness exhibited through the presence of the micro-structured interface is likely to be dependent on the mechanical properties of the bulk adherends. In the current analysis, polycarbonate was modelled without a damage criterion as no adherend failure was observed in our previous experimental work. Although not explored here, the elastic modulus of the structured adherend is likely to have an important influence also. Again, higher stiffness features tend to increase load capacity, but reduce displacement and thereby probably reduce toughness.

Table 3
ANOVA analysis parameters for joint load capacity (top dataset), strain to failure (middle dataset) and work-to-failure (bottom dataset).

Load Capacity					
Source	DF	SS	F-Value	P-Value	%
Feature width	2	18370	12.7	3e-4	13.7
Channel width	2	47617	32.8	5e-7	35.4
Aspect ratio	2	53981	37.2	2e-7	40.1
Error	20	14524			10.8
Strain-to-failure					
Source	DF	SS	F-Value	P-Value	%
Feature width	2	8.1	164.9	3e-13	44.8
Channel width	2	2.4	48.1	2e-8	13.1
Aspect ratio	2	7.1	144.9	1e-12	39.4
Error	20	0.5			2.7
Work-to-failure					
Source	DF	SS	F-Value	P-Value	%
Feature width	2	16341	114.43	1E-11	44.7
Channel width	2	8823	61.78	2.75E-09	24.1
Aspect ratio	2	9968	69.8	9.5E-10	27.3
Error	20	1428			3.9

When considering the wider viability for this micro-structuring approach, it is also important to consider costs, speed of manufacture and versatility. The creation of the tooling required for the micro-fabrication approach is certainly somewhat complex. In addition, using the current mould insert materials, the micro-structured components can only be manufactured in thermoplastic polymers such as e.g. polycarbonate (PC), poly ether-ether ketone (PEEK) and polypropylene (PP). To overcome this limitation, it is possible to modify the mould insert fabrication process to create a nickel-based insert via the LIGA process, to enable metal-injection moulding to be realised, but this is beyond the scope of the present study. To illustrate the potential viability of micro-structuring adhesive joints more economically, an initial 3D-printing-based manufacturing method was investigated.

3.4. 3D printing of micro-structured joints: a potentially more practical approach

The approach previously utilised for fabrication of the micron-scale interlocking (<100 μm feature size) relies on expensive and complex machinery including photolithography, dry etching machinery, nanoimprint-lithography, and injection moulding tooling. A potentially more cost-effective avenue to achieve micro-structured joints is via 3D-printing. This approach would enable rapid joint production at lower cost with comparatively simpler machinery. 3D printing also opens up the possibility of easily varying the mechanical properties along the bond-line and better tailoring the joint performance.

Thus, a preliminary study has been conducted using a Form 2 printer (Formlabs Inc., USA). The 3D-printing is achieved through stereolithography (SLA) based curing of layers. The designed part is created using computer aided design (CAD) software and subsequently uploaded to the printer in the form of a stereolithography (STL) file. In the SLA printing approach, a laser source is directed via a galvanometer, hitting mirrors to position the laser perpendicular to the build platform. Scans are determined in a pre-defined manner, according to the dimension within the STL design file. The laser photopolymerises the resin (stored within the resin tank), with the part created in a layer-by-layer manner attached to the build platform. When compared to other 3D-printing technologies such as fused deposition modelling (FDM) and selective laser sintering (SLS), the SLA-based approach offers substantially greater resolution. In this work, the Formlabs Grey Pro engineering resin was used. Conventional tensile tests on dog-bone type specimens were performed to obtain the key material properties. These are shown in Table 4 and this material data was also used to model the 3D printed joints using the FE approach discussed above. Adherends were printed and bonded together using the same protocol used for the previous experiments. A representative image showing the 3D-printed square-wave features is given in Fig. 7.

From quantification work, it was estimated that printing resolution was limited to around 200 μm [25]. A mechanical testing study on the effect of aspect ratio was performed with feature widths of $\lambda_f = 300$ μm and $\lambda_f = 600$ μm used in combination with feature depths of 150 μm, 300 μm and 600 μm to produce aspect ratios of 0.5, 1 and 2, respectively. A control experiment with no structuring was also included with the adherend surfaces roughened with P80 sandpaper prior to assembly to provide a benchmark for comparison. An additional joint type was also produced, this time having a variation of aspect ratio along the bond line. Narrower, more compliant features (AR = 2.0) were placed at the edges and stiffer features (AR = 1.0) were positioned centrally. It was hypothesised that the hybrid design would possess lower stiffness

Table 4
Material properties for the tough Grey Pro resin (Formlabs Inc., USA) obtained via tensile testing.

Young's Modulus (GPa)	UTS (MPa)	Failure strain (%)
2.6	65	19.4

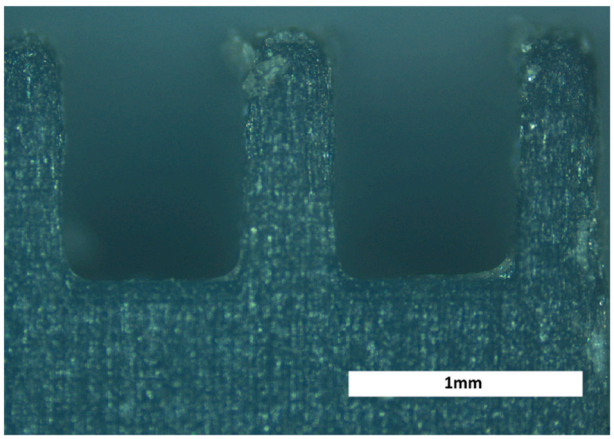

Fig. 7. Optical image of the AR = 2 3D printed specimens pre-assembly.

features near the edges of the joint, mitigating the detrimental near-edge peak stresses that typically lead to failure of the joint. Additionally, the results from Fig. 6 indicate that the AR = 1 case is best for load capacity, but AR = 2 was optimal for energy absorption. Hence, the aim here is also to tailor the joint to have a desirable compromise between both. A schematic illustrating the structure of the hybrid feature interface is given in Fig. 8. Simulations were also conducted for comparison with the experimental results. The same FE modelling approach (i.e. interlocking joint with frictional contact) as outlined in Section 2 was used again here with the elastic-plastic properties for the Grey Pro resin obtained from the tensile test data in Table 4.

The experimental force versus strain results for the 3D printed joints are plotted in Fig. 9. As expected, the structured joints (Fig. 9b–e) perform better than the planar roughened joint (Fig. 9a) in terms of load capacity (up to three times better). The mean experimental results are shown in Fig. 10 together with the corresponding simulation results.

The experimental results for the structured joints (in Figs. 9 and 10) again illustrate that aspect ratio has a clear effect on load capacity, as well as, strain-to-failure and work-to-failure. The AR = 0.5 test group results in lower values of load capacity and strain-to-failure. This is again likely due to reduced interlocking associated with the lower feature depth and issues upon joint assembly. Load capacity then increases as we move to the AR = 1.0 group as the feature depth is now sufficient to facilitate effective interlocking and compressive loading as well as enabling effective bending interaction of features. Increasing the aspect ratio further to AR = 2.0 causes the load capacity to drop off as these longer, thinner features are significantly less stiff. For strain-to-failure (Fig. 10b) and work-to-failure (Fig. 10c), a progressive increase was noted with increasing aspect ratio. This is likely to be simply because higher aspect ratios are less stiff (in bending) and lead to more joint displacement resulting in greater strain and greater work done.

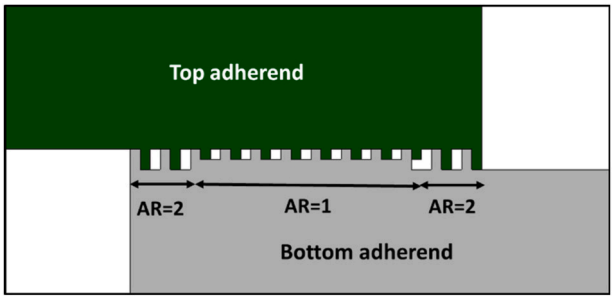

Fig. 8. Schematic of the 3D printed joint offering variable hybrid feature options (in this case, two feature types) along the bond line. Here, the more compliant Aspect Ratio 2 is placed near the edges and the stiffer Aspect Ratio 1 is used in the central region.

Recall that the hybrid feature case (with AR = 2.0 at the edges and AR = 1.0 in the central region), was designed to tailor the joint to have a desirable compromise between load capacity and energy absorption (toughness). Indeed, we can see clearly from the results in Fig. 10 that the hybrid aspect ratio case (with AR = 1.0 & AR = 2.0) has load capacity, strain-to-failure and work-to-failure that are intermediate between the AR = 1.0 and AR = 2.0 results. Thus, the hybrid aspect ratio yields an improvement in the toughness properties (work-to-failure) relative to the AR = 1.0 group, whilst retaining greater load capacity than the AR = 2.0 category.

Broadly speaking, the FE results in Fig. 10 exhibit the same key trends as the experiments although there are some discrepancies in the magnitudes predicted. A source of difference between experiment and model in this particular case might be attributed to the inherent variation in 3D printed feature geometry relative to the more precise microfabrication strategies used earlier, with the printed features having a propensity to be printed slightly wider than designed. Reflecting on the strain-to-failure simulation data, it appears that the simulations generally over-predict joint extension (Fig. 10b), apart from the variable feature width group. A corresponding over-prediction is present for work-to-failure in Fig. 10c. The over-prediction here can be accounted for due to the contact definitions within the model assuming perfect contact for each interlocking site. Under these idealised conditions, full feature bending is realised leading to elevated strain values. A further limitation associated with the model was the lack of fracture data implemented for the grey pro resin. This would explain the disparity for the AR = 1.0 group where failure was primarily driven through a bulk failure (as we shall see later in Fig. 11c) at comparably lower strain values (~4% - see Fig. 9c). On the other hand, greater bending and extension were permitted in the simulations. In summary, the strain-to-failure and work-to-failure values were consistently lower in experiments compared to the simulation data and this is attributed to the rapid failure/facture typically observed during the tests (with bulk fracture observed especially for AR = 1.0). This contrasts with the experimental findings for the more ductile polycarbonate testing presented earlier, reaffirming the requirement of ductile adherends for optimal loading response.

Through the course of testing, different failure mechanisms were observed (Fig. 11), with adhesive failure observed commonly for the samples failing at lower loads such as the AR = 0.5 group (Fig. 11a), indicating that reduced interlocking suppressed the constraining effect that yields the mechanical improvement. For samples that failed at higher loads, the predominant failure mechanism was via mixed adhesive/bulk adherend failure (Fig. 11b) and bulk failure (Fig. 11c), emanating at the edges of the bond-line and propagating across the entirety of the bonded joint. This (bulk) failure mechanism was not observed for the lower aspect ratio results. For AR = 1.0, failure typically occurred through fracture of the bulk grey pro resin first (Fig. 11c) indicating that the mechanical properties at the interface exceed the mechanical properties of the grey pro resin used. The hybrid joint type, on the other hand, tended to exhibit a consistent cohesive-based failure pathway (without bulk failure). This is likely due to the more compliant AR = 2.0 features near the edges permitting more displacement and reducing peak stresses.

Therefore, we have demonstrated that the hybrid joint can give a compromise of properties between the high load capacity of AR = 1.0 and the high energy absorption of AR = 2.0 while also avoiding the detrimental bulk fracture observed for the AR = 1.0 case. This suggests that the 3D printing approach has good potential to be used in spatially tailoring joints for optimum mechanical properties (as well as being more rapid and cost effective). This is a preliminary study and further improvement is possible. For instance, the main drawback of the SLA-based 3D printing route used here is the minimum feature size being limited to 200–300 μm. It is likely that reducing the feature size further would increase the capability of the method by increasing the accuracy with which specific features could be deployed in particular regions –

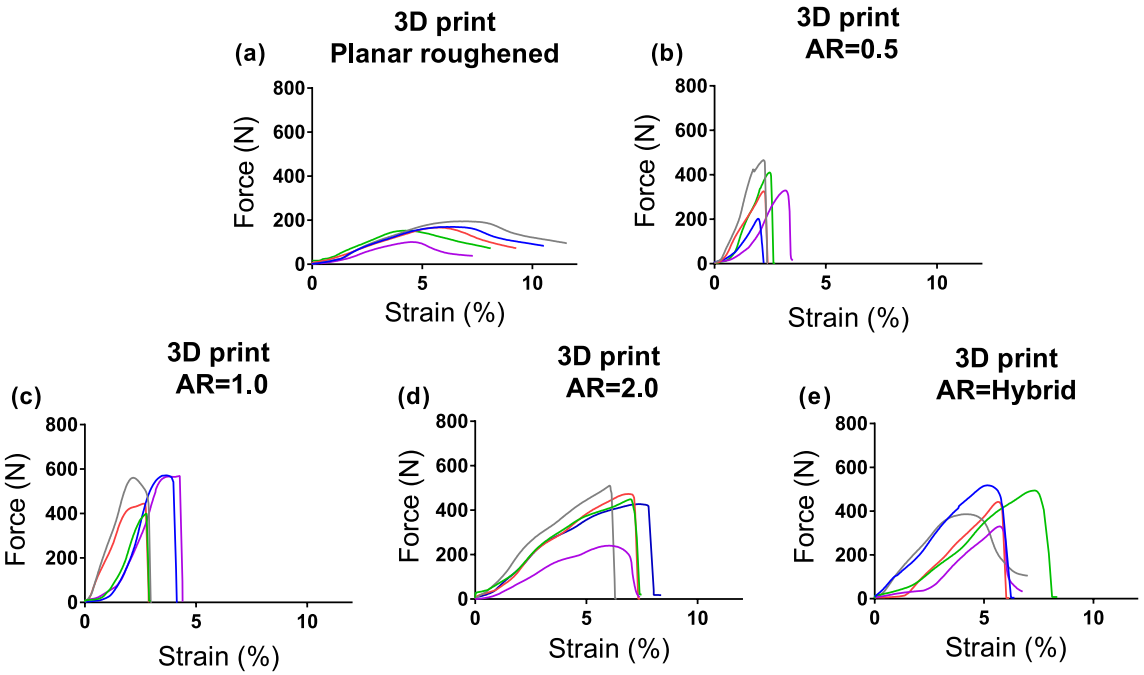

Fig. 9. Force versus strain for all 3D printed joints: (a) unstructured, planar roughened, (b) all features at AR = 0.5, (c) all features at AR = 1, (d) all features at AR = 2, and (e) hybrid with AR = 2 at edges and AR = 1 in the centre. Different line colours represent five repeat tests under identical conditions.

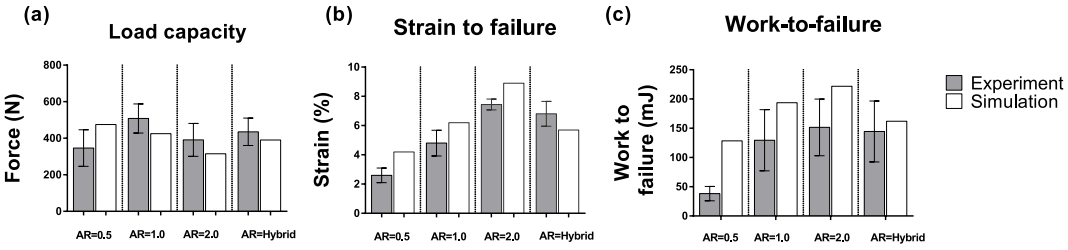

Fig. 10. Bar plots comparing mean experimental results (grey) with simulation (white) for the 3D printed joints: (a) load capacity, (b) strain-to-failure and (c) work-to-failure. Error bars represent (± SD).

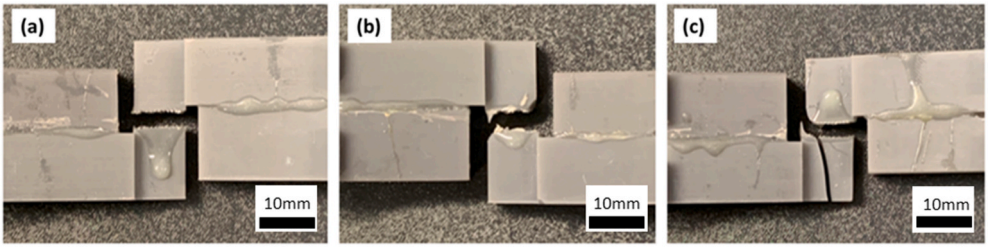

Fig. 11. Typical observed joint failures: (a) Conventional adhesive-based failure typical of the weaker joints with AR = 0.5, (b) mixed-failure with partial bulk failure observed for intermediate strength joints with AR = 2, and (c) complete bulk failure as exhibited for the stronger, better performing joints with AR = 1.

such as the near-edge parts of the bond-line where the peak stresses occur and through introducing a substantially greater number of high density, high aspect ratio features at the very edges of the joint.

4. Conclusions

Approaches to optimising the mechanical performance of structured single-lap joints based on interlocking adherends have been explored via experiment and finite element (FE) analysis. The experimental joints were produced using a modified nanoimprint-lithography and injection moulding process. The FE modelling showed that, with frictional contact alone (i.e. no adhesive present), the simulations were within 6.9% and −12.7% of the mean experimental results for joint load capacity. This indicates that mechanical interlocking (via the progressive bending interaction between interlocking features as identified in Ref. [17]) accounts for the majority of the load carrying capacity of the joints explored. In theory, this opens up the new possibility of adhesive-less joints as long as sufficient lateral constraint (or clamping) is maintained to hold the joint together. The model was then used in conjunction with a design of experiments approach using Taguchi analysis to establish how various microstructured geometrical parameters (feature width, channel width and feature aspect ratio (AR)) affect the

mechanical performance. Feature aspect ratios of AR = 0.5, 1.0 and 2.0 where explored. Load capacity was found to increase roughly proportional to feature width (due to stiffer features). The converse trend was observed for channel width (due to decreased density of features). Work-to-failure values (an indicator of toughness) increased with aspect ratio in-line with features becoming more compliant and permitting more displacement during bending. For load capacity, an intermediate aspect ratio of AR = 1.0 was optimal. Lower aspect ratios (e.g. AR = 0.5) posed difficulties for achieving effective interlocking, while higher aspect ratios (e.g. AR = 2.0) resisted less load due again to reduced feature stiffness. Overall, for joints having a single feature type, an aspect ratio AR = 1.0 was found to give an optimal comprise between load capacity and work-to-failure. The relative contributions of each of the parameters was further quantified by employing a three-way ANOVA analysis which highlighted aspect ratio as having the biggest effect on joint load capacity. Finally, it was demonstrated that an SLA-based 3D printing approach can be used to vary feature parameters along the bond line to tailor mechanical properties. A hybrid joint-type containing both AR = 2.0 features at the edges and AR = 1.0 features in the central potion exhibited mechanical properties intermediate between those for joints with only AR = 1.0 or AR = 2.0 features. Thus, the hybrid joint had higher load capacity than AR = 2.0 together with greater energy absorption than AR = 1.0. The hybrid 3D printed joint also avoided the bulk brittle failure that tended to occur in the AR = 1.0 joints. The 3D printing approach is highly attractive as it is likely to be considerably more versatile and cost effective compared to the micro-fabrication processes and affords the option of varying feature properties along the bond-line.

Declaration of competing interest

The authors declare that they have no known competing financial interests or personal relationships that could have appeared to influence the work reported in this paper.

Data availability

Data will be made available on request.

Acknowledgements

The authors would like to acknowledge the support of the Leverhulme Trust for supporting the work under project grant “Fundamental Mechanical Behaviour of Nano and Micro Structured Interfaces” (RPG-2017-353) and the EPSRC for providing an EPSRC-DTG PhD studentship (EP/N509668/1) for the first author. Personnel at the James Watt Nanofabrication Centre (JWNC) at the University of Glasgow are also thanked for their invaluable technical support.

References

[1] Alfano M, et al. Surface patterning of metal substrates through low power laser ablation for enhanced adhesive bonding. J Adhes 2014;90(5–6):384–400.
[2] Zhang XM, Yue TM, Man HC. Enhancement of ceramic-to-metal adhesive bonding by excimer laser surface treatment. Mater Lett 1997;30(April):327–32.
[3] Palmieri FL, et al. Laser ablative surface treatment for enhanced bonding of Ti-6Al-4V alloy. ACS Appl Mater Interfaces 2013;5:1254–61.
[4] Banea MD, Da Silva LFM. Adhesively bonded joints in composite materials: an overview. Proc Inst Mech Eng Part L J Mater Des Appl 2009;223(1):1–18.
[5] Kim KS, Yoo JS, Yi YM, Kim CG. Failure mode and strength of uni-directional composite single lap bonded joints with different bonding methods. Compos Struct 2006;72(4):477–85.
[6] Kumar S, Wardle BL, Arif MF. Strength and performance enhancement of bonded joints by spatial tailoring of adhesive compliance via 3D printing. ACS Appl Mater Interfaces 2017;9(1):884–91.
[7] Ubaid J, Wardle BL, Kumar S. Strength and performance enhancement of multilayers by spatial tailoring of adherend compliance and morphology via multimaterial jetting additive manufacturing. Sci Rep 2018;8(1):1–10.
[8] Maloney K, Fleck N. Tear resistance of a square-wave joint: experiment versus cohesive zone model. Int J Adhesion Adhes 2018;84:9–17.
[9] Maloney K, Fleck N. Damage tolerance of an architected adhesive joint. Int J Solid Struct 2017;1:1–11. 0.
[10] Cordisco FA, Zavattieri PD, Hector LG, Carlson BE. Mode i fracture along adhesively bonded sinusoidal interfaces. Int J Solid Struct 2016;83:45–64.
[11] Corbett MC, Sharos PA, Hardiman M, McCarthy CT. Numerical design and multi-objective optimisation of novel adhesively bonded joints employing interlocking surface morphology. Int J Adhesion Adhes 2017;78:111–20.
[12] O’Brien M, Mortell DJ, Corbett MC, O’Higgins RM, McCarthy CT. Mechanical performance and failure behaviour of miniature aluminium joints with novel interlocking reinforcement. Int J Adhesion Adhes 2019;95(August).
[13] Ramaswamy K, O’Higgins RM, Corbett MC, McCarthy MA, McCarthy CT. Quasi-static and dynamic performance of novel interlocked hybrid metal-composite joints. Compos Struct 2020;253(July):112769.
[14] Haghpanah B, Chiu S, Vaziri A. Adhesively bonded lap joints with extreme interface geometry. Int J Adhesion Adhes 2014;48:130–8.
[15] Yukimoto Y, Matsuzaki R, Todoroki A. Mode II interfacial fracture toughness of composite/adhesive interfaces obtained by in-mold surface modification. Int J Adhesion Adhes 2014;50:191–8.
[16] Hikosaka Y, Matsuzaki R, Todoroki A, Mizutani Y. Enhancement of interfacial fracture toughness of carbon/epoxy composite adhesive joints by in-mold surface preparation. Express Polym Lett 2012;7(3):293–303.
[17] Hamilton A, Xu Y, Kartal ME, Gadegaard N, Mulvihill DM. International Journal of Adhesion and Adhesives Enhancing strength and toughness of adhesive joints via micro-structured mechanical interlocking. Int J Adhesion Adhes 2021;105:102775. November 2020.
[18] Hamilton A, Perris J, Convery N, Mulvihill DM, Gadegaard N. Flexible inserts for injection molding of complex micro-structured polymer components. Macromol Mater Eng 2021:1–21.
[19] Bin Jaber S, Hamilton A, Xu Y, Kartal ME, Gadegaard N, Mulvihill DM. Friction of flat and micropatterned interfaces with nanoscale roughness. Tribol Int 2021;153:106563. July 2020.
[20] Perris J, Xu Y, Kartal ME, Gadegaard N, Mulvihill DM. Tailorable and repeatable normal contact stiffness via micropatterned interfaces. Tribol Lett 2021;69(3):1–12.
[21] Roy S, et al. Plastic deformation of steel plates under high impact loading. 2013.
[22] [Online]. Available: Polycarbonate www.chemeurope.com/en/encyclopedia/Polycarbonate.html. [Accessed 29 March 2022].
[23] Sethuramiah A, Kumar R. Statistics and experimental design in perspective. 2016.
[24] Araldite rapid datasheet: hunstaman advanced materials. 2011.
[25] Convery N, Samardzhieva I, Stormonth-Darling JM, Harrison S, Sullivan GJ, Gadegaard N. 3D printed tooling for injection molded microfluidics. Macromol Mater Eng 2021;306(11):1–11.